Optimization of CNTs growth on TiB_2-based composite powders by CVD with Fe as catalyst

Jia Lin [a,b,*], Yihang Yang [a], Houan Zhang [a], Bo Su [b], Yulin Yang [a]

[a] Fujian Key Laboratory of Functional Materials and Applications, School of Materials Science and Engineering, Xiamen University of Technology, Xiamen 361024, China

[b] Bristol Dental School, University of Bristol, Bristol BS1 2LY, UK

Abstract

Carbon nanotubes (CNTs) are successfully grown on the surface of TiB_2 matrix by chemical vapor deposition with Fe as catalyst. However, CNT growth has to be improved before conducting integration procedures. The effects of synthesis conditions on the structure of CNT(Fe)–TiB_2 are evaluated by scanning electron microscopy, transmission electron microscopy, and Raman spectroscopy. Results indicate that with an increase in synthesis temperature, carbon yield increases because of the improvement in the initial growth rate of CNTs. The morphology of as-received carbon changes due to changes in surface roughness of TiB_2. With an increase in Fe catalyst, the density and diameter of carbon particles increase as well because of the increased number of activity sites and agglomeration of Fe particles. As the gas flow rate of methane supply rises, the density and length of CNTs initially increase and then decrease. This behavior is attributed to the increase in carbon diffusion rate and decrease in contact time between the catalyst and the carbon precursor. As growth duration is extended, CNT growth initially improves because of the sufficient reaction time between the carbon precursor and the catalyst. However, the quality of CNTs subsequently decreases, and a large amount of amorphous carbon is produced owing to the aggregation of the carbon precursor, which leads to excessive concentration of Fe.

Keywords: B. Composites; B. Spectroscopy; D. Borides; E. Structural applications

Corresponding author: Jia Lin

E-mail: jiajia10182003@163.com

Tel/Fax: +86-592-6291325

1 Introduction

Among the borides of titanium, titanium diboride (TiB_2) possesses excellent chemical and physical properties, such as high refractoriness, high hardness, high modulus, low thermal expansion, superior chemical stability, and good thermal and electrical characteristics [1–3]. Thus, TiB_2-based ceramics have been regarded as a potential material for structural and functional applications. However, TiB_2-based ceramics exhibits intrinsic brittleness, which impedes their practical application [4, 5]. Many studies have reported that adding reinforcement into TiB_2 matrix can improve its mechanical performance. These reinforcements include metallic additives (Ni [6], Fe [7], Co [8], etc.) and non-metallic additives ($TiSi_2$ [9], $MoSi_2$ [10], SiC [11], etc.). As a characteristic determined by brittleness, the fracture toughness of TiB_2-based ceramics can only be enhanced to 8 $MPa \cdot m^{1/2}$, which is far inadequate for practical use.

To address this shortcoming, a method of reinforcement that can not only toughen the TiB_2 matrix but also shows no harmful reaction with the TiB_2 matrix has to be developed. Owing to their highly distinct mechanical properties, carbon nanotubes (CNTs) have been recognized for their potential to effectively enhance phase-change materials [12, 13]. The tensile strength of CNTs can be 100 times higher than that of steel; however, the density of CNTs is only one-sixth that of steel [14]. CNTs exhibit considerably high toughness because they are composed of a large number of C=C covalent bonds [15]. In our previous study [16], we mixed TiB_2 and CNTs directly by powder metallurgy. The fracture toughness of TiB_2–CNTs was found to be 9.4±0.2 $MPa \cdot m^{1/2}$—that is, higher than that of pure TiB_2 ceramics. However, CNTs reportedly agglomerate at the TiB_2 grain junctions, impeding the efficient use of the toughening effect of CNTs. Thus, a method that allows CNTs to be evenly dispersed in the

TiB_2 matrix has to be identified.

Compared with traditional synthesis, chemical vapor deposition (CVD) is a promising technique for CNT growth *in situ* that relies on the decomposition of hydrocarbons with the use of catalysts deposited on substances [17, 18]. Studies have suggested that CVD can disperse CNTs uniformly in metallic, ceramic, and polymeric matrices [19–21]. Yang et al. [22] reported on the use of CVD to synthesize Al matrix composites reinforced with CNTs grown *in situ*. Huang et al. [23] proved that CNT–ZnO composite materials with improved field-emission characteristics could be successfully grown by thermal CVD. However, few studies have explored the use of CVD to synthesize TiB_2-based composites with self-grown CNTs. In this regard, we have investigated the feasibility of CNTs grown on TiB_2 powder by CVD with Fe as catalyst [24]. Results showed that CNTs could be successfully synthesized on the surface of TiB_2 powders and that the amount of Fe catalyst and synthesis temperature affect the growth rate of the resulting CNTs. A study reported that CNT formation on TiB_2 by using Fe as catalyst was achieved at 900 °C–950 °C, and the number of CNTs increased with an increase in Fe catalyst. The performance of grown CNTs can be controlled by the morphology of the catalyst, type of hydrocarbon precursors, gas flow, growth time, and temperature. High growth temperature can accelerate the initial growth rate of CNTs, and a greater quantity of the Fe catalyst can further decompose carbonaceous precursors. However, high processing temperature can lead to grain coarsening, and excessive Fe can cause performance degradation in TiB_2. Efforts must be devoted toward lowering the growth temperature of CNTs and reducing the quantity of the Fe catalyst. The present study focuses on the improvement of CNT growth by adjusting gas flow and growth time. Scanning electron microscopy (SEM), transmission electron microscopy (TEM), and Raman spectroscopy were used to characterize the variations in CNTs. By analyzing the relationship between the synthesis conditions and the microstructure of the CNT/TiB_2 composite powder

grown *in situ*, the optimal synthesis conditions can be determined.

2 Experimental

Commercially available TiB_2 powder (1–2 μm, purity > 99.9%, Shanghai ST-Nano Science & Technology Co. Ltd., China), $Fe(NO_3)_3{\cdot}9H_2O$ (98.5%, Analytical Reagent, Sigma–Aldrich), and NaOH (0.8 g, 0.02 mol, 99.9% purity) were used as starting materials. The CNT(Fe)–TiB_2 powder was prepared using the same method mentioned in a previous study [24], with certain modifications. Reports [17, 25-28] enumerate four successive steps included in the mechanism of CNT growth: (1) surface absorption of carbon, (2) dissolution/segregation of carbon species, (3) carbon diffusion through catalytic particles, and (4) carbon deposition to form CNTs. Thus, the synthesis conditions that affect these four steps can influence the formation of CNTs. Among various influencing factors for CNT growth, Fe content, synthesis temperature, growth duration, and methane supply were identified as the main factors. The synthesis process is thus presented in detail:

First, $Fe(NO_3)_3{\cdot}9H_2O$ and TiB_2 powder were directly mixed in distilled water. The NaOH solution was then added to the mixture, with constant stirring, to obtain a ($Fe(OH)_3$–TiB_2) slurry. The weight of $Fe(NO_3)_3{\cdot}9H_2O$ was determined for Fe content adjustment (5 wt%, 10 wt%, or 15 wt%) in the final composite powder. The slurry was subsequently dried in a vacuum furnace at 80 °C for 24 h and then calcined in N_2 (300 $mL{\cdot}min^{-1}$, 99.99% purity) at 400 °C for 2 h to obtain Fe_2O_3–TiB_2 powder. To synthesize the CNTs, the Fe_2O_3–TiB_2 powder was placed in the CVD system. Fe_2O_3 was reduced at 600 °C in hydrogen (100 $mL{\cdot}min^{-1}$, 99.99% purity) and then transformed into elementary Fe. The as-received Fe-TiB_2 powder was ultimately heated to a synthesis temperature (700 °C, 800 °C, or 900 °C) for a certain growth duration (120 min, 150 min, or 180 min) with the methane supply (50 $mL{\cdot}min^{-1}$, 100 $mL{\cdot}min^{-1}$, or 150 $mL{\cdot}min^{-1}$) to promote the growth of CNTs. After growth, carbon yield was calculated as follows:

$$\text{Carbon yield (\%)} = \frac{m_1 - m_2}{m_2} \times 100\% \quad (1)$$

where m_1 is the weight of the as-received CNT(Fe)–TiB_2 powder (g), and m_2 is the weight of the Fe–TiB_2 catalyst (g).

SEM (ZEISS EVO18, Germany) with energy-dispersive spectroscopy (Oxford Instruments X-Max^N, UK) was conducted to observe the morphology and purity of the as-received CNT(Fe)–TiB_2 powders. High- and low-resolution TEM (Tecnai G^{2}F30 TEM, 300 kV) was employed to characterize the microstructure of the grown CNTs. The average grain size was determined using the linear intercept method. The phase compositions of the powders were detected by X-ray diffraction (PANalytical X'Pert PRO, Holland, CuKα=1.5418 Å). Raman spectroscopy was conducted using the 532 nm line of an Ar^+ laser as the excitation source to identify the crystallinity of the CNTs in the composite powders.

3 Results and discussion

Fig. 1 presents the SEM images of the CNT(Fe)–TiB_2 powders under different synthesis temperatures (700 °C, 800 °C, and 900 °C). As shown in Fig. 1a, some very fine round particles are distributed on the surface of the TiB_2 powders synthesized at 700 °C; the carbon yield is as low as 1.19%. In Fig. 1b, the granular object on the surface of the TiB_2 matrix becomes less apparent as the synthesis temperature is increased to 800 °C. High temperature likely increases the fluidity of the Fe catalyst. Short CNTs emerge, indicating that CNT growth has started, as can be observed in Fig. 1b. Carbon yield is calculated to be 5.54%. When the synthesis temperature is increased to 900 °C, carbon yield increases to 9.95%, the CNTs grow longer, and more become evenly distributed, as seen in Fig. 1c. On the basis of the theories referred to in Ref.[17], the initial growth rate of CNTs is influenced by the synthesis temperature. A higher synthesis temperature indicates a higher initial growth rate, which can extend growth duration to ensure the growth process of CNTs. Meanwhile, the surface roughness of the TiB_2 matrix changes with an increase in temperature, which is an

important factor affecting the surface absorption of carbon and the dissolution/segregation of carbon species, resulting in carbon of different forms.

To evaluate the effect of Fe content on CNT growth, Fig. 2 presents the morphology and structure of CNTs grown with different Fe contents (5 wt%, 10 wt%, and 15 wt%) observed by SEM. As known, the catalyst deposited on the surface of the TiB_2 powder can provide nucleation sites for CNT growth. The carbon yield calculated using Formula (1) rises from 2.77% to 9.95% as Fe content is increased from 5 wt% to 15 wt%. As shown in Fig. 2a, intact CNTs become hardly apparent because the Fe content is only 5 wt%, which provides less activity sites for CNT growth. In Fig. 2b, no CNTs are visible when the Fe content is increased to 10 wt%; however, the quantity of round particles attached to the surface of TiB_2, which has Fe particles inside and a graphite layer on the outside, increases. In Fig. 2c, some CNTs are visible, and the density and diameter of the carbon particles increase as the Fe content increases to 15 wt%. This phenomenon is attributed to the effect of catalytic particles. A larger amount of catalyst indicates the presence of a larger number of activity sites for carbon diffusion; however, an excessive amount of catalyst can cause agglomeration of Fe particles, inducing an increase in the diameter of the catalytic particles. These results are consistent with the analysis in our previous study [24].

To achieve excellent performance of the finished ceramic product, the catalyst content has to be reduced and the synthesis temperature lowered. As factors influencing the formation of CNTs, changes in methane supply are investigated. Fig. 3 presents the SEM images of CNT(Fe)–TiB_2 powders with different gas flow rates (50 $mL \cdot min^{-1}$, 100 $mL \cdot min^{-1}$, and 150 $mL \cdot min^{-1}$). As shown in Figs. 3a–3b, the density of the as-grown CNTs rises as the gas flow rate is increased from 50 $mL \cdot min^{-1}$ to 100 $mL \cdot min^{-1}$, but the carbon yield decreases (Fig.4). Meanwhile, the CNTs formed at a lower gas flow rate of 50 $mL \cdot min^{-1}$ are shorter and more entangled, as shown in Fig. 3a. According to a previous study [17], there is sufficient time for

deposition between the carbon precursor and the Fe catalyst at a low gas flow rate (e.g., 50 $mL \cdot min^{-1}$) for carbon to be attracted onto the surface of Fe catalysts and thus form multiple layers of graphitic wall or amorphous carbon. Given the low gas flow rate, the carbon wall is abnormally increased owing to the denaturation of the catalyst particles, eventually causing the denaturation of the layers. As the gas flow rate increases to 100 $mL \cdot min^{-1}$, more CNTs, which are longer and less entangled, are distributed on the surface of TiB_2, as shown in Fig. 3b. According to Ref.[17], methane supply at a higher gas flow rate can provide a greater opportunity for a carbon precursor to react with catalysts to form more CNTs, promoting carbon diffusion through catalytic particles (as shown in Fig. 3b); on the contrary, a higher gas flow rate can also result in reduced contact time between the carbon precursor and the Fe catalyst. In Fig. 3c, no CNTs are found as the gas flow rate rises to 150 $mL \cdot min^{-1}$ because of the insufficient decomposition rate of methane, thus depressing carbon deposition to form CNTs and reducing the corresponding carbon yield (Fig. 4).

The morphology of CNTs is rather different, as observed in Fig. 3. The structure of as-grown CNTs is further investigated. Fig. 5 presents the TEM images of the CNT(Fe)–TiB_2 powders with methane supply at different gas flow rates. The diameter of CNTs decreases from 85 nm to 55 nm as the gas flow rate of methane supply is increased from 50 $mL \cdot min^{-1}$ to 100 $mL \cdot min^{-1}$. Numerous impurities are attached to the wall of the CNTs when the gas flow rate is 50 $mL \cdot min^{-1}$ (Fig. 5a), which is consistent with the SEM analysis result. The duration of carbon absorption on the surface at such a low gas flow rate (50 $mL \cdot min^{-1}$) is prolonged, causing the layer of the carbon wall to undergo denaturation. As the gas flow rate of methane rises to 100 $mL \cdot min^{-1}$, there is sufficient time for carbon layer formation and CNT growth; however, less impurities and denatured CNT walls are found in Fig. 5b because the Fe catalysts are less susceptible to poisoning. Finally, as the gas flow rate of methane is increased to 150 $mL \cdot min^{-1}$, the Fe particles are coated with carbon layers, as shown in Fig.

5c, which is attributed to the insufficient time for methane decomposition, thus depressing CNT growth.

Fig. 6 shows the Raman spectra of the CNT(Fe)–TiB_2 with methane supply at different gas flow rates. Two distinct peaks appear on the curve—D-peak and G-peak. D-peak at about 1344.61 cm^{-1} is related to the disordered bands induced by the amorphous carbon, disordered graphite, and carbon impurities on the surface of the CNTs. G-peak at about 1591.43 cm^{-1} is related to the stretching vibrations of C=C bond. The intensity ratios of D and G-peaks (I_D/I_G) are calculated to estimate the degree of graphitization of the CNTs. When methane supply is increased from 50 $mL \cdot min^{-1}$ to 100 $mL \cdot min^{-1}$, I_D/I_G decreases from 1.08 to 1.01; as the methane supply is further increased to 150 $mL \cdot min^{-1}$, I_D/I_G increases from 1.01 to 1.02. A lower I_D/I_G indicates a more highly crystallized graphite, less amorphous carbon, disorder-induced carbon, and presence of impurities. The 2D-peaks (observed at 2701.56 cm^{-1}), indicating the presence of denatured carbon walls, decrease as the gas flow rate is reduced. All results are consistent with the SEM and TEM analysis results, suggesting that the carbon yield is slightly reduced, but the quality of the as-grown CNTs with a methane supply of 100 $mL \cdot min^{-1}$ is improved.

To further improve the morphology of the CNTs, the growth duration was studied. The SEM images of the CNT(Fe)–TiB_2 with different growth durations (120 min, 150 min, or 180 min) are compared in Fig. 7. As shown in Figs. 7a and 7b, the density of the CNTs sharply rises as the growth duration is increased from 120 min to 150 min, together with an increase in carbon yield (Fig. 8). Growth duration affects the contact time between the methane and the catalyst, directly influencing carbon deposition to form CNTs [17]. A longer growth duration ensures sufficient reaction time between the methane and the catalyst to allow CNTs to grow well with increased purity and crystallized graphite. Meanwhile, the quality and length of the CNTs also increase as the growth duration is extended from 120 min to 150 min.

These increases are attributed to the extended residence time of the active Fe catalysts in the carbon precursor. Methane concentration rises with time, which can provide a good medium for CNT growth. However, as the growth duration exceeds 150 min and is further increased to 180 min, the CNTs become short and entangled, and a large amount of amorphous carbon is produced, as shown in Fig. 7c. This finding is attributed to the aggregation of methane gas over such a long duration, resulting in excessive methane concentration. High levels of methane can subject the catalysts to poisoning and prompt the emergence of denatured carbon walls and amorphous carbon.

Fig. 9 presents the TEM images of CNT(Fe)–TiB_2 synthesized at 150 min. Compared with those synthesized at 120 or 180 min, the CNTs obtained at 150 min exhibit good hollowness. The surface of the carbon wall is likely to be smoother with higher purity. Multiple graphitized layers are observed in the HRTEM image in Fig. 9b. The interlayer spacing is about 0.34 nm, which is consistent with the (002) crystal face spacing of graphite. Consistent with a previous analysis, a sufficient time for methane–catalyst reaction is important to reduce the length and amount of CNTs with a well-graphitized wall and form fewer impurities.

Fig. 10 presents a comparison of the Raman spectra of CNT(Fe)–TiB_2 with different growth durations. As growth duration is extended from 120 min to 150 min, I_D/I_G decreases from 1.01 to 0.94, indicating that the purity and crystallization of the CNTs are improved. When the growth duration is extended to 180 min, I_D/I_G is is 1.06, which is considerably larger than the value obtained when the growth duration is set to 150 min. This result is rather consistent with the SEM and TEM analysis results. Owing to the excessive growth duration, the methane concentration increases, leading to increases as well in amorphous carbon and denatured graphitic layers.

4. Conclusions

By using Fe as a catalyst, CNTs were successfully grown on the surface of TiB_2 by CVD. To improve the growth of the CNTs, the effects of synthesis conditions (Fe content, synthesis temperature, growth duration, and methane supply), including the structure of CNT(Fe)–TiB_2, are evaluated. This study mainly aims to achieve enhanced CNT growth with reduced Fe content and lowered synthesis temperature. The conclusions drawn are as follows:

(1) With increased synthesis temperature, the initial CNT growth rate rises, which indicates an extension in the growth duration of the CNTs. In addition, high temperature can influence the fluidity of the Fe catalyst, causing changes in the surface roughness of the TiB_2 matrix, which is an important factor affecting the form of as-received carbon.

(2) With increased Fe catalyst, more activity sites become available for carbon diffusion, which is favorable for CNT growth. However, an excessive quantity of catalyst can cause agglomeration of Fe particles, thereby increasing the density and diameter of carbon particles.

(3) With increased gas flow rate of methane supply, the carbon precursor has a greater opportunity to react with the catalysts to form more CNTs initially so that the CNTs are thinner and longer when the gas flow rate is increased to 100 $mL \cdot min^{-1}$. However, as the gas flow rate is further increased, the contact time between the carbon precursor and the Fe catalyst decreases, resulting in the insufficient decomposition rate of methane. Thus, no CNTs are obtained as the gas flow rate is increased to 150 $mL \cdot min^{-1}$, and carbon yield decreases.

(4) With increased growth duration, the carbon precursor and the catalyst have sufficient reaction time, resulting in well grown CNTs with high purity and crystallized graphite. The quality and length of CNTs also improves as the growth duration is extended from 120 min to 150 min. However, when the growth duration exceeds 150 min, the CNTs become short and entangled, and a large amount of amorphous carbon is generated. This

occurrence is attributed to the aggregation of the carbon precursor, leading to excessive concentration. The catalysts then become susceptible to poisoning, and denatured carbon walls and amorphous carbon emerge.

In conclusion, the optimal synthesis condition for CNT growth in the TiB_2 matrix using Fe as the catalyst by CVD is as follows: Fe content, 10 wt%; synthesis temperature, 800 °C; growth duration, 150 min; and gas flow rate of methane supply, 100 $mL \cdot min^{-1}$.

Acknowledgements

This work was supported by the National Natural Science Foundation of China (51772253), the Fujian Natural Science Foundation (2018J01523), the Foundation for Outstanding Young Talents in Higher Education of Fujian Province (2015), the Program for New Century Excellent Talents in University of Fujian Province (2016), and the Program for Innovative Research Team in Science and Technology in Fujian Province University (IRTSTFJ), China.

References

[1] M.M. Mokhayer, M.G. Kakroudi, S.S. Milani, H. Ghiasi, N.P. Vafa, Investigation of AlN addition on the microstructure and mechanical properties of TiB_2 ceramics, Ceram. Int. 45 (2019) 16577–16583.

[2] Z. Wang, B. Xie, W. Zhou, G. Shi, Z. Wu, Thermophysical properties of TiB_2\SiC ceramics from 300 °C to 1700 °C, Int. J. Refract. Met. Hard Mater. 41 (2013) 609–613.

[3] F. Shayesteh, S.A. Delbari, Z. Ahmadi, M. Shokouhimehr, M.S. Asl, Influence of TiN dopant on microstructure of TiB_2 ceramic sintered by spark plasma, Ceram. Int. 45 (2019) 5306–5311.

[4] Z. Yin, J. Yuan, W. Xu, K. Liu, S. Yan, Graphene nanosheets toughened TiB_2-based ceramic tool material by spark plasma sintering, Ceram. Int. 44 (2018) 8977–8982.

[5] X. Liu, J. Pei, M. Liu, Z. Wang, L. Liu, L. Jing, Z. Wu, Microstructure and mechanical properties of textured TiB_2 ceramic fabricated by combination of catalyst and hot-forging,

Mater. Chem. Phys. 200 (2017) 217–222.

[6] H. Wang, B. Wang, S. Li, Q. Xue, F. Huang, Toughening magnetron sputtered TiB_2 coatings by Ni addition, Surf. Coat. Technol. 232 (2013) 767–774.

[7] Z. Hadjem-Hamouche, K. Derrien, E. Héripré, J.P. Chevalier, In-situ experimental and numerical studies of the damage evolution and fracture in a Fe-TiB_2 composite, Mater. Sci. Eng. A 724 (2018) 594–605.

[8] Z. Fu, R. Koc, Pressureless sintering of TiB_2 with low concentration of Co binder to achieve enhanced mechanical properties, Mater. Sci. Eng. A 721 (2018) 22–27.

[9] B.R. Golla, B. Basu, Hot-pressed TiB_2–10 wt.% $TiSi_2$ ceramic with extremely good thermal transport properties at elevated temperatures (up to 1273 K), Scripta Mater. 68 (2013) 79–82.

[10] T.S.R.Ch. Murthy, R. Balasubramaniam, B. Basu, A.K. Suri, M.N. Mungole, Oxidation of monolithic TiB_2 and TiB_2–20 wt.% $MoSi_2$ composite at 850 °C, J. Eur. Ceram. Soc. 26 (2006) 187–192.

[11] F. Ghafuri, M. Ahmadian, R. Emadi, M. Zakeri, Effects of SPS parameters on the densification and mechanical properties of TiB_2-SiC composite, Ceram. Int. 45 (2019) 10550–10557.

[12] A. Haque, R. Sachan, J. Narayan, Synthesis of diamond nanostructures from carbon nanotube and formation of diamond-CNT hybrid structures, Carbon 150 (2019) 388–395.

[13] V. Dhand, S.K. Hong, L. Li, J.M. Kim, S.H. Kim, K.Y. Rhee, H.W. Lee, Fabrication of robust, ultrathin and light weight, hydrophilic, PVDF-CNT membrane composite for salt rejection, Composites Part B 160 (2019) 632–643.

[14] J. Cha, G.H. Jun, J.K. Park, J.C. Kim, H.J. Ryu, S.H. Hong, Improvement of modulus, strength and fracture toughness of CNT/Epoxy nanocomposites through the functionalization of carbon nanotubes, Composites Part B 129 (2017) 169–179.

[15] Y.A. Lv, Y.H. Cui, Y.Z. Xiang, J.G. Wang, X.N. Li, Modulation of bonding between noble metal monomers and CNTs by B-, N-doping, Comput. Mater. Sci. 48 (2010) 621–625.

[16] W. Chen, J. Lin, Y. Yang, H. Zhang, Microstructure and mechanical properties of TiB_2-CNTs composites prepared by spark plasma sintering, Sci. Adv. Mater. 10 (2018) 1782–1787.

[17] Y. Yang, H. Zhang, Y. Yan, Synthesis of CNTs on stainless steel microfibrous composite by CVD: Effect of synthesis condition on carbon nanotube growth and structure, Composites Part B 160 (2019) 369–383.

[18] C. Hoecker, F. Smail, M. Pick, A. Boies, The influence of carbon source and catalyst nanoparticles on CVD synthesis of CNT aerogel, Chem. Eng. J. 314 (2017) 388–395.

[19] A.V. Radhamani, H.C. Lau, S. Ramakrishna, CNT-reinforced metal and steel nanocomposites: A comprehensive assessment of progress and future directions, Composites Part A 114 (2018) 170–187.

[20] Li Zhu, X. Dong, M. Xu, F. Yang, M.D. Guiver, Y. Dong, Fabrication of mullite ceramic-supported carbon nanotube composite membranes with enhanced performance in direct separation of high temperature emulsified oil droplets, J. Membr. Sci. 582 (2019) 140–150.

[21] M.R. Zakaria, H.M. Akil, M.H.A. Kudus, F. Ullah, F. Javed, N. Nosbi, Hybrid carbon fiber-carbon nanotubes reinforced polymer composites: A review, Composites Part B 176 (2019) 107313.

[22] X. Yang, T. Zou, C. Shi, E. Liu, C. He, N. Zhao, Effect of carbon nanotube (CNT) content on the properties of in-situ synthesis CNT reinforced Al composites, Mater. Sci. Eng. A 660 (2016) 11–18.

[23] C.S. Huang, C.Y. Yeh, Y.H. Chang, Y.M. Hsieh, C.Y. Ku, Q.T. Lai, Field emission properties of CNT–ZnO composite materials, Diamond Relat. Mater. 18 (2009) 452–456.

[24] J. Lin, Y. Yang, H. Zhang, Y. Yang, S. Hu, Effects of synthesis temperature and Fe catalyst amount on the performance of in situ CNTs/TiB_2 composites, J. Alloys Compd. 745 (2018) 817–824.

[25] H. Khodja, M. Pinault, M. Mayne-L'Hermite, C. Reynaud, Carbon nanotube growth mechanism investigated by ion beam analysis, Nucl. Instrum. Methods Phys. Res., Sect. B 249 (2006) 523–526.

[26] Y. Zhang, K.J. Smith, A kinetic model of CH_4 decomposition and filamentous carbon formation on supported Co catalysts, J. Catal. 231 (2005) 354–364.

[27] K. Liu, K. Jiang, C. Feng, Z. Chen, S. Fan, A growth mark method for studying growth mechanism of carbon nanotube arrays, Carbon 43 (2005) 2850–2856.

[28] D. Chen, R. Lødeng, A. Anundskås, O. Olsvik, A. Holmen, Deactivation during carbon dioxide reforming of methane over Ni catalyst: microkinetic analysis, Chem. Eng. Sci. 56 (2001) 1371–1379.

Figure captions:

Fig.1 Secondary electron SEM images of CNT(Fe)-TiB_2 powders under different synthesis temperature:(a) 700°C, (b) 800°C and (c) 900°C. (Fe content, 15 wt%; growth duration, 120 min; and gas flow rate of methane supply, 150 $mL \cdot min^{-1}$)

Fig.2 Secondary electron SEM images of CNT(Fe)-TiB_2 powders with different Fe contents:(a) 5 wt%, (b) 10 wt% and (c) 15 wt%. (synthesis temperature, 900 °C; growth duration, 120 min; and gas flow rate of methane supply, 150 $mL \cdot min^{-1}$)

Fig.3 Secondary electron SEM images of CNT(Fe)-TiB_2 powders with different gas flow rates:(a) 50 $mL \cdot min^{-1}$, (b) 100 $mL \cdot min^{-1}$ and (c) 150 $mL \cdot min^{-1}$. (Fe content, 10 wt%; synthesis temperature, 800 °C; and growth duration, 120 min)

Fig.4 Carbon yield of CNT(Fe)-TiB_2 powders with different gas flow rates. (Fe content, 10

wt%; synthesis temperature, 800 °C; and growth duration, 120 min)

Fig.5 TEM images of CNT(Fe)-TiB_2 powders with different gas flow rates:(a) 50 $mL \cdot min^{-1}$, (b) 100 $mL \cdot min^{-1}$ and (c) 150 $mL \cdot min^{-1}$. (Fe content, 10 wt%; synthesis temperature, 800 °C; and growth duration, 120 min)

Fig.6 Raman spectra of CNT(Fe)-TiB_2 powders with different gas flow rates. (Fe content, 10 wt%; synthesis temperature, 800 °C; and growth duration, 120 min)

Fig.7 Secondary electron SEM images of CNT(Fe)-TiB_2 powders with different growth durations:(a) 120 min, (b) 150 min and (c) 180 min. (Fe content, 10 wt%; synthesis temperature, 800 °C; and gas flow rate of methane supply, 100 $mL \cdot min^{-1}$)

Fig.8 Carbon yield of CNT(Fe)-TiB_2 powders with different growth durations. (Fe content, 10 wt%; synthesis temperature, 800 °C; and gas flow rate of methane supply, 100 $mL \cdot min^{-1}$)

Fig.9 TEM images of the product formed over TiB_2 powders with 10 wt% Fe at 800 °C for 150 min.

Fig.10 Raman spectra of CNT(Fe)-TiB_2 powders with different growth durations. (Fe content, 10 wt%; synthesis temperature, 800 °C; and gas flow rate of methane supply, 100 $mL \cdot min^{-1}$)

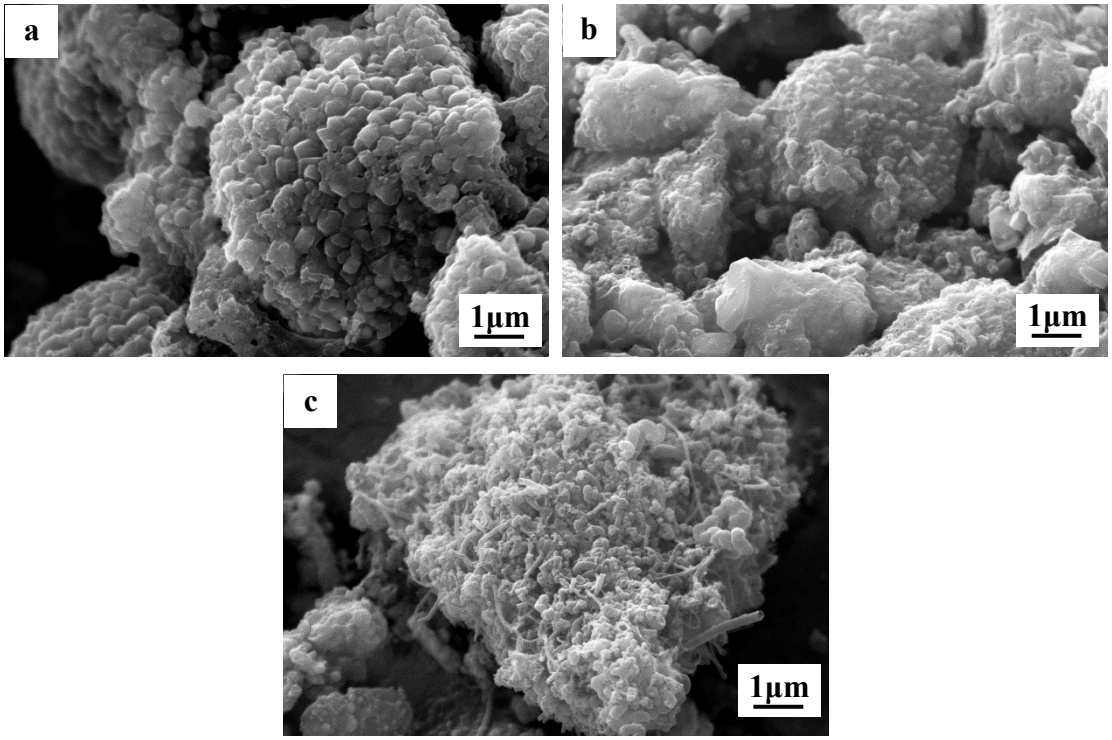

Fig.1 Secondary electron SEM images of CNT(Fe)-TiB_2 powders under different synthesis temperature:(a) 700°C, (b) 800°C and (c) 900°C. (Fe content, 15 wt%; growth duration, 120 min; and gas flow rate of methane supply, 150 $mL \cdot min^{-1}$)

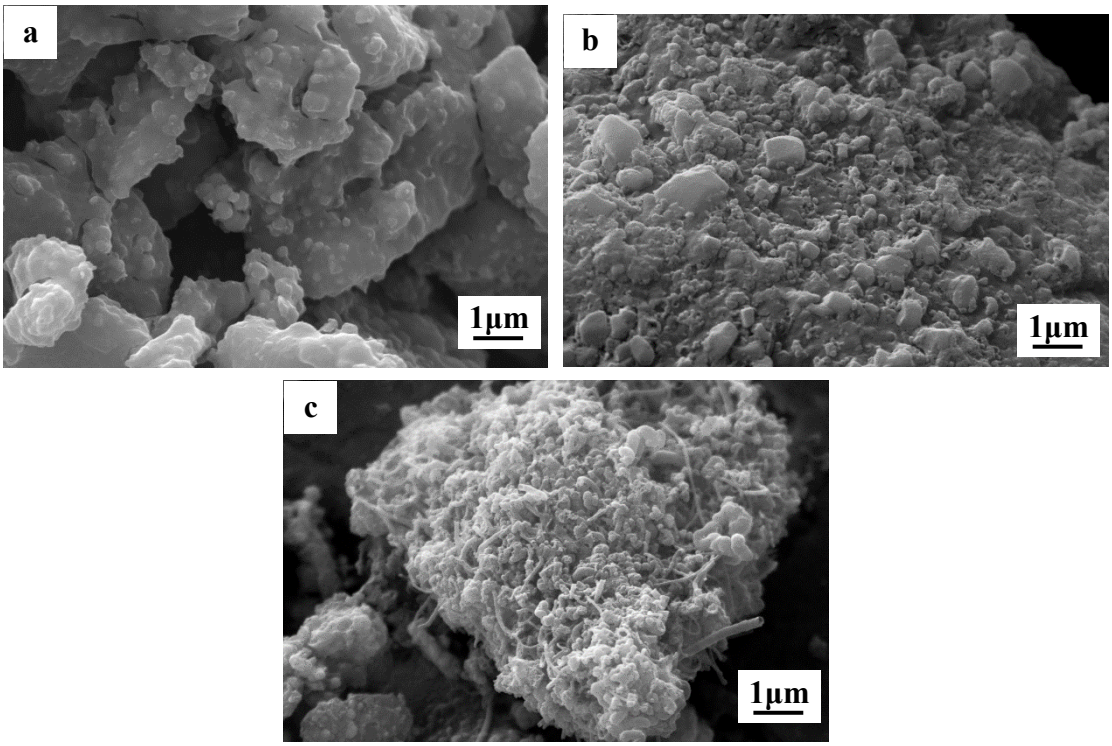

Fig.2 Secondary electron SEM images of CNT(Fe)-TiB_2 powders with different Fe contents:(a) 5 wt%, (b) 10 wt% and (c) 15 wt%. (synthesis temperature, 900 °C; growth duration, 120 min; and gas flow rate of methane supply, 150 $mL \cdot min^{-1}$)

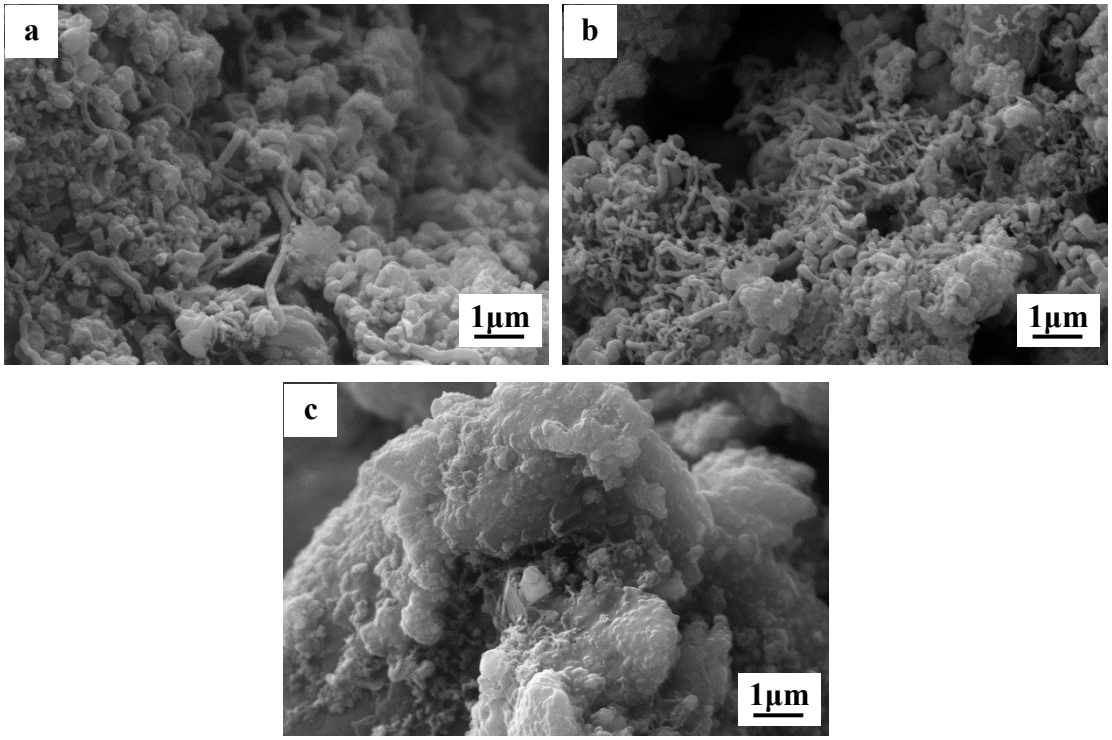

Fig.3 Secondary electron SEM images of CNT(Fe)-TiB_2 powders with different gas flow rates:(a) 50 $mL \cdot min^{-1}$, (b) 100 $mL \cdot min^{-1}$ and (c) 150 $mL \cdot min^{-1}$. (Fe content, 10 wt%; synthesis temperature, 800 °C; and growth duration, 120 min)

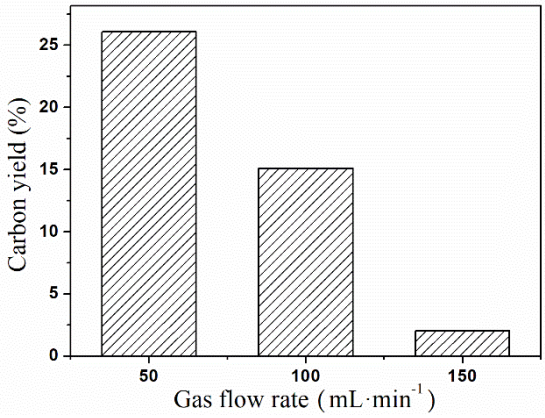

Fig.4 Carbon yield of CNT(Fe)-TiB_2 powders with different gas flow rates. (Fe content, 10 wt%; synthesis temperature, 800 °C; and growth duration, 120 min)

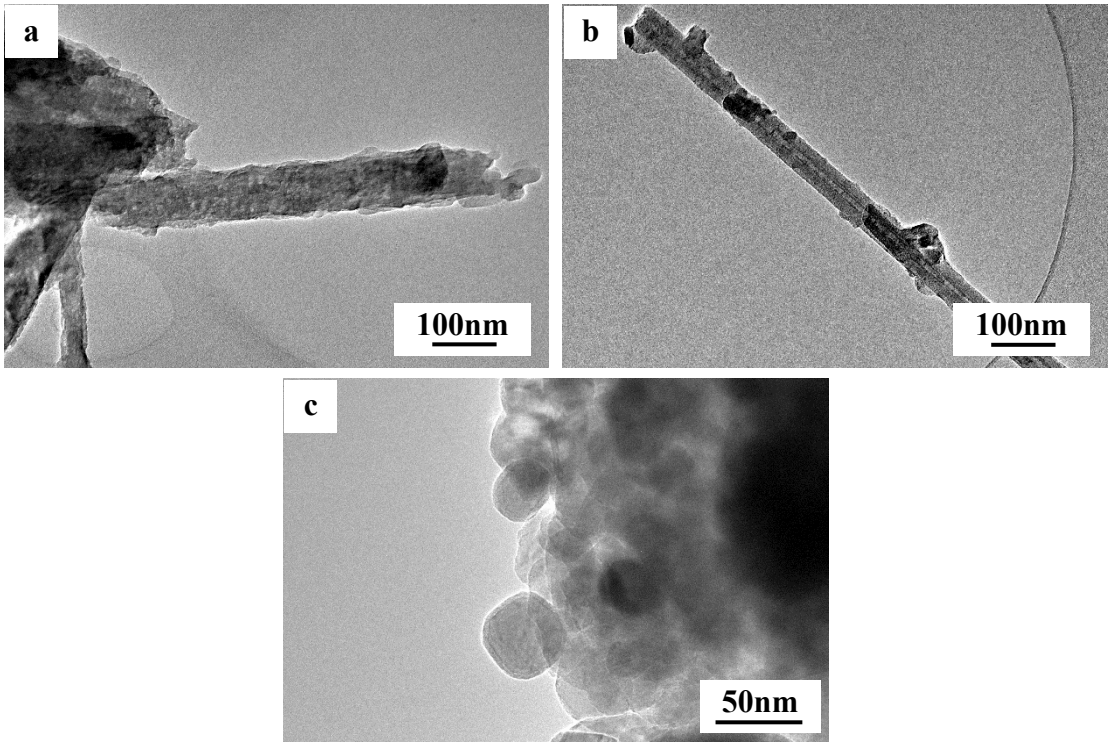

Fig.5 TEM images of CNT(Fe)-TiB_2 powders with different gas flow rates:(a) 50 $mL \cdot min^{-1}$, (b) 100 $mL \cdot min^{-1}$ and (c) 150 $mL \cdot min^{-1}$. (Fe content, 10 wt%; synthesis temperature, 800 °C; and growth duration, 120 min)

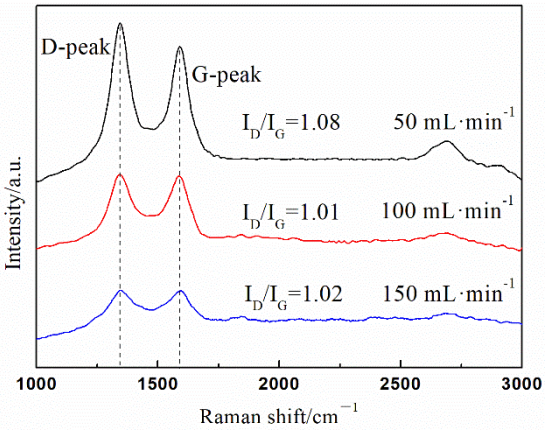

Fig.6 Raman spectra of CNT(Fe)-TiB_2 powders with different gas flow rates. (Fe content, 10 wt%; synthesis temperature, 800 °C; and growth duration, 120 min)

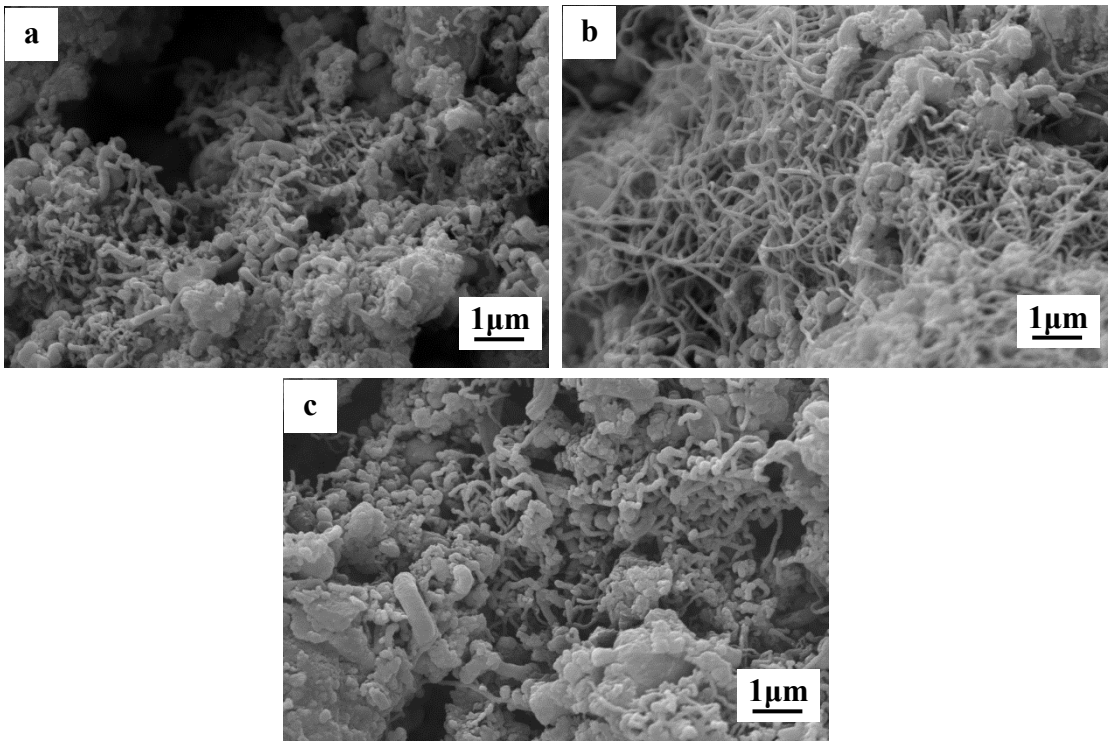

Fig.7 Secondary electron SEM images of CNT(Fe)-TiB_2 powders with different growth durations:(a) 120 min, (b) 150 min and (c) 180 min. (Fe content, 10 wt%; synthesis temperature, 800 °C; and gas flow rate of methane supply, 100 $mL \cdot min^{-1}$)

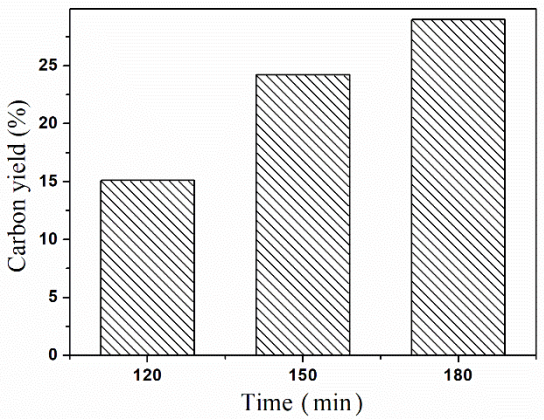

Fig.8 Carbon yield of CNT(Fe)-TiB_2 powders with different growth durations. (Fe content, 10 wt%; synthesis temperature, 800 °C; and gas flow rate of methane supply, 100 $mL \cdot min^{-1}$)

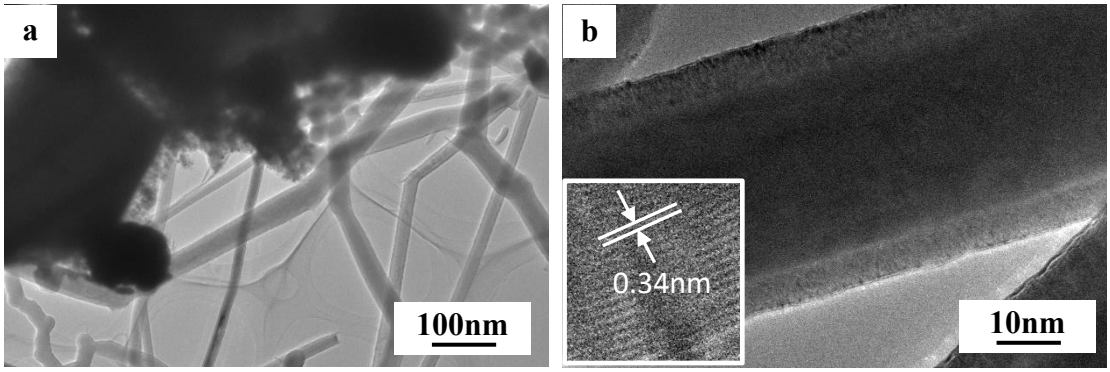

Fig.9 TEM images of the product formed over TiB_2 powders with 10 wt% Fe at 800 °C for 150 min.

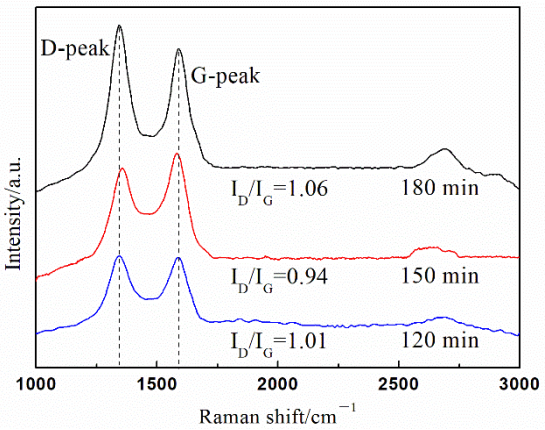

Fig.10 Raman spectra of CNT(Fe)-TiB_2 powders with different growth durations. (Fe content, 10 wt%; synthesis temperature, 800 °C; and gas flow rate of methane supply, 100 mL·min^{-1})